# The autocorrelation function and fluctuations of the soft X-ray sky on scales from 1 arcmin to 5°

L.-W. Chen,[1] A. C. Fabian,[1] R. S. Warwick,[2] G. Branduardi-Raymont[3] and C. R. Barber[2]

[1] *Institute of Astronomy, Madingley Road, Cambridge CB3 0HA*
[2] *X-ray Astronomy Group, Physics Department, University of Leicester, Leicester LE1 7RH*
[3] *Mullard Space Science Laboratory, University College London, Holmbury St Mary, Dorking, Surrey RH5 6NT*

## ABSTRACT

We investigate the spatial anisotropy and inhomogeneity of the soft X-ray sky, using one field of deep exposure and six collinear fields of medium exposure observed with the *ROSAT* Position Sensitive Proportional Counter. We first remove time-variable contaminations and excise bright sources from the data, followed by simultaneous spectral fitting to determine the diffuse extragalactic X-ray background count rate; we then reconstruct the strip composed of the six medium fields which span $2°$ (RA)$\times 7°$ (Dec.) of the sky. Using the deep field and the merged strip, we calculate the weighted angular autocorrelation function and the rms fluctuation of the surface intensity of the X-ray sky in the energy band $\sim 0.4$–$2.4$ keV from 1 arcmin to 5°. The $2\sigma$ upper limit to excess fluctuation on scales down to a few arcmin is found to be lower than 20 per cent. As a result of using the low extragalactic background count rate determined from spectral fitting, the $2\sigma$ upper limits on the autocorrelation function are similar to previous values, some of which cover a higher energy band and some of which use a higher estimate of the extragalactic X-ray background (due to various contaminations or to the presence of brighter discrete sources). The weighted fitting of the observed autocorrelation function to a theoretical power-law model scaling as $\theta^{-0.8}$ reduces the uncertainty and yields a $2\sigma$ upper limit $= 3.86 \times 10^{-3} \theta^{-0.8}$ over the scale of $\theta = 2$–300 arcmin. It implies that the sources contributing the residual soft X-ray background must have a correlation length $r_0 < 2\ h_{50}^{-1}$ Mpc if they lie at redshifts $< 1$, otherwise in general $r_0 < 4\ h_{50}^{-1}$ Mpc.

**Key words:** diffuse radiation – large-scale structure of Universe – X-rays: general.

## 1 INTRODUCTION

The isotropy of the X-ray background (XRB) is a diagnostic of its origin and of the homogeneity of the nearby Universe (Fabian & Barcons 1992 and references therein). The main contributors to small-scale spatial fluctuations in the XRB are sources that are just unresolved. Studies of the distribution of such fluctuations [the $P(D)$ distribution; Scheuer 1974] can therefore be used to obtain the source counts to levels well below those at which direct counts are possible (see Georgantopoulos et al. 1993; Hasinger et al. 1993; Barcons et al. 1994 for recent applications of this technique to *ROSAT* data; and Butcher et al. 1994 for *Ginga* data). There may also be an excess variance due to the effects of

source clustering or large-scale structure, or to new classes of sources that do not contribute simply to the $P(D)$ distribution (for example, sources that are very extended). In this paper, we obtain strong constraints on excess fluctuations in the soft X-ray sky from the angular autocorrelation function (ACF) and from the dependence of the fluctuation amplitude on angular scale.

Previous work on the ACF has been carried out in the 2–10 keV band with the *HEAO-1* A2 instrument (Persic et al. 1989; Martín-Mirones et al. 1991; Mushotzky 1992), the 4–12 keV band with the *Ginga* LAC (Carrera et al. 1991, 1993), the 0.3–3.5 keV band of the *Einstein* Observatory (Barcons & Fabian 1989; Soltan 1991) and the 0.9–2.4 keV band of *ROSAT* (Hasinger, Schmidt & Trümper 1991). The

ACF is defined as

$$W(\theta) = \frac{\langle \delta I \delta I_\theta \rangle}{\langle I \rangle^2}, \quad (1)$$

where $I$ is the intensity at one position, and $I_\theta$ is the intensity at a second position offset by an angle $\theta$ from the first. The best X-ray results give upper limits of $W(\theta) \lesssim 10^{-4}$ on scales of $2°$ or more and a detection of $W(\theta) \sim 3 \times 10^{-5}$ on a scale of about $10°$ (Mushotzky 1992). The use of imaging telescopes in the softer band means that the soft X-ray ACF can be extended down to a scale of a few arcmin where $W(\theta)$ is less than a few times $10^{-3}$ (e.g. Hasinger 1992). Limits on excess fluctuations ($\delta I/I$), obtained by comparing the predictions of an extrapolation of the direct source counts to the observed $P(D)$ distribution, range from a few per cent on scales of a few degrees in the harder band to about 100 per cent on the few-arcmin scale in the soft band (see figs 5 and 6 in Fabian & Barcons 1992 for plots of excess fluctuations and the ACF amplitude as a function of angular scale).

Here we measure the ACF and excess fluctuations in the 0.4–2.4 keV band from one deep (exposure time 69 ks), and six overlapping and collinear medium (exposure times of 13 to 21 ks), survey fields obtained with *ROSAT*. All fields lie at high Galactic latitude in regions of low interstellar column density. Before computing $W(\theta)$ or $\delta I/I$ of the residual XRB, we must first remove all detectable X-ray sources from the fields and contaminating backgrounds which would otherwise dominate the results.

## 2 DATA REDUCTION

### 2.1 The data and instrumental effects

The fields were observed with the Position Sensitive Proportional Counter (PSPC) on *ROSAT* and are fully described in the work by Branduardi-Raymont et al. (1994), where the direct source counts are reported. A $P(D)$ analysis of the fields is given by Barcons et al. (1994). The deep (DS) field is centred at RA (2000) $13^h34^m37^s$, Dec. (2000) $37°54'44''$ ($b \approx 75°.9$); the medium fields (MS) are centred at RA $10^h10^m15^s.8$ and Dec. from $50°45'14''$ to $55°45'14''$ ($b \approx 49°.4-51°.5$), the centres being $1°$ apart in Dec. The medium and deep fields are shown before and after the processing needed to remove bright sources (described below) in Figs 1 and 2, respectively. In the present paper, we have numbered the MS fields from 1 to 6 from north to south.

The PSPC is a gas detector with a thin plastic window which is supported against the pressure differential by a thin-wire grid, which in turn is held in place by metal ribs. These ribs leave a central 40-arcmin-diameter region unobscured and divide the outer annulus of the field of view into eight sectors (the field of view has a full diameter of $2°$). During an observation, the whole satellite is wobbled by a few arcmin in order that no point source near the centre of the field, where the point spread function (PSF) is most sharp, is completely obscured by the thin wire grid. This results in a blurred imprint of the rib structure on the image. In the present analysis, the areas of the image subject to such blocking have been masked by fitting a rib model to the data and replacing the count rate in the affected pixels by a bad-data flag (we use a mask function with ribs of at least 7-arcmin width to take account of the blurring). After removal of the non-vignetted component, the theoretical vignetting function (*ROSAT* AO-2 manual) for 1 keV has been fitted to the radial profile of each field, and the data corrected for the vignetting effects. This initial image analysis was conducted using a pixel size of $15 \times 15$ arcsec$^2$. In the present paper, we assume a power-law spectrum of energy index 1 for bright sources and use a count-to-flux conversion of 1 PSPC count s$^{-1}$ (0.4–2.4 keV)$^{-1} = 1.23 \times 10^{-11}$ erg cm$^{-2}$ s$^{-1}$ for both MS and DS fields, where the column density $N_H$ is $\sim 6.5-9 \times 10^{19}$ cm$^{-2}$ (Stark et al. 1992). The corresponding conversion rate for the XRB depends on the model adopted for the XRB spectrum (see Section 2.5).

### 2.2 Modelling the data

The detected counts are due to the extragalactic XRB, the Galactic soft XRB, cosmic X-ray sources, cosmic-ray events, and solar X-rays scattered by the Earth's atmosphere (SSX), and some may possibly have an unknown origin, e.g. the short-term (which may be associated with auroral X-rays) and long-term enhancements (Snowden et al. 1993a). We are interested in the spatial fluctuations of the first of these, and hereafter use 'XRB' when referring to this diffuse extragalactic component (to define the XRB further in terms of its spectral form, see Section 2.5). The observed count $C_{x,y}^k$ in a pixel $x, y$ with a solid angle $A$ and an exposure time $t_{exp}^k$ in field $k$ is therefore modelled by a combination of a vignetted term, including diffuse and point sources, and an unvignetted, non-XRB term $R_{PB}^k$:

$$C_{x,y}^k = t_{exp}^k \left\{ R_{PB}^k + V_{x,y}^k \left[ (R_{XRB} + R_{vig}^k) A \right. \right.$$
$$\left. \left. + \sum_{x',y'} f_{PSF}(x, y, x', y') S_{x,y} \right] \right\}, \quad (2)$$

where $V_{x,y}^k$ is the vignetting factor depending on the distance from the field centre, and $x, y$ are the sky coordinates (RA, Dec.). The first vignetted term, $R_{XRB}$, refers to the XRB signal of interest here, with $R_{vig}^k$ representing the other non-extragalactic backgrounds (i.e. the Galactic diffuse emission and atmospheric contributions) which have no cosmological significance. The last term represents the presence of discrete sources; the contribution from $S_{x,y}$ to $C_{x,y}^k$ depends on the shape of the detector/mirror PSF $f_{PSF}(x, y, x', y')$. In the present analysis, source counts in the extended tail of the PSF which may extend beyond the bounds of the assumed detection cells are ignored (since they are insignificant), so that each detection cell is regarded as an independent bin (see Section 2.4). All the backgrounds are assumed to be intrinsically spatially uniform, although the non-extragalactic sources of the background ($R_{vig}^k$ and $R_{PB}^k$) are likely to differ from field to field, in particular the highly time-variable SSX component (Snowden & Freyberg 1993) and the cosmic ray induced background (Snowden et al. 1992; Plucinsky et al. 1993). It is therefore important to correct for these contaminations which may either dilute or enhance the spatial fluctuations, especially when merging the overlapping fields. We describe below how, in addition to removing bright sources, we attempt to determine the best value of the diffuse extragalactic XRB rate from the data.
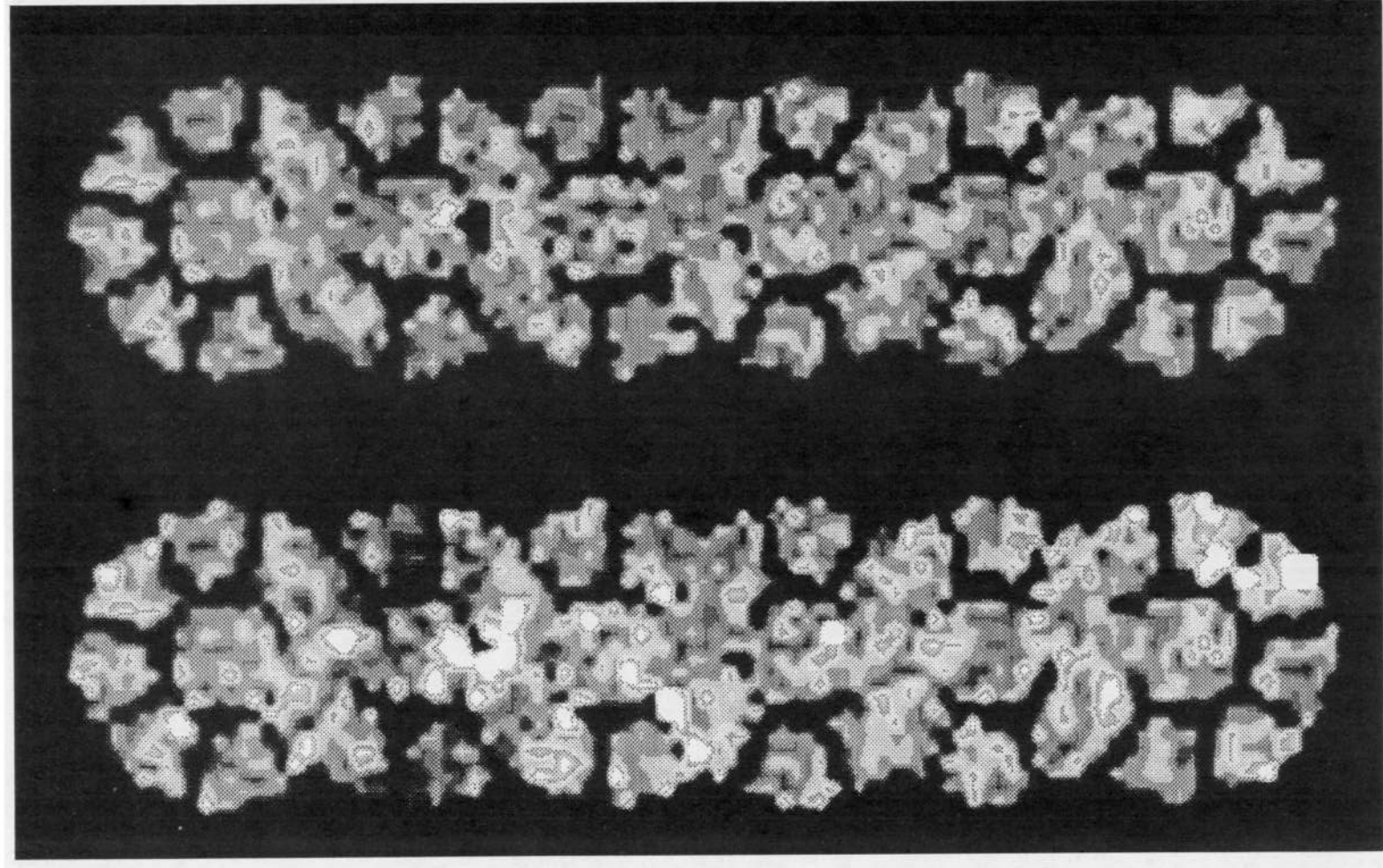
**Figure 1.** The merged strip of six medium survey fields in the 0.4–2.4 keV band before (left panel) and after (right panel) removing sources brighter than ~ $5 \times 10^{-14}$ erg cm$^{-2}$ s$^{-1}$; the cosmic ray induced background has been subtracted from each image, the image devignetted and normalized to 20 ks, and finally all the vignetted contaminations removed. The size of each image is 2° (RA) × 7° (Dec.), composed of the six inner 45-arcmin-radius regions of the MS fields numbered 1–6 from top to bottom. The levels of the intensity are linearly scaled and limited to ~ 15 count arcmin$^{-2}$ (20 ks)$^{-1}$ to enhance the background structure, whereas some bright sources [with intensity values of up to 65 count arcmin$^{-2}$ (20 ks)$^{-1}$] can be seen in the left panel, including a bright diffuse source appearing in the upper middle (~ the centre of Field 2) which is identified as a low-surface-brightness cluster and will be reported on elsewhere (Warwick et al., in preparation). The darkest area indicates missing data, i.e. where a bright source has been removed or the window-supporting structure blocks the data. Note that bright sources have been removed on a finer pixel scale (1 arcmin square) than shown here, where the unit pixel is 4 arcmin square.

© **Royal Astronomical Society** • **Provided by the NASA Astrophysics Data System**
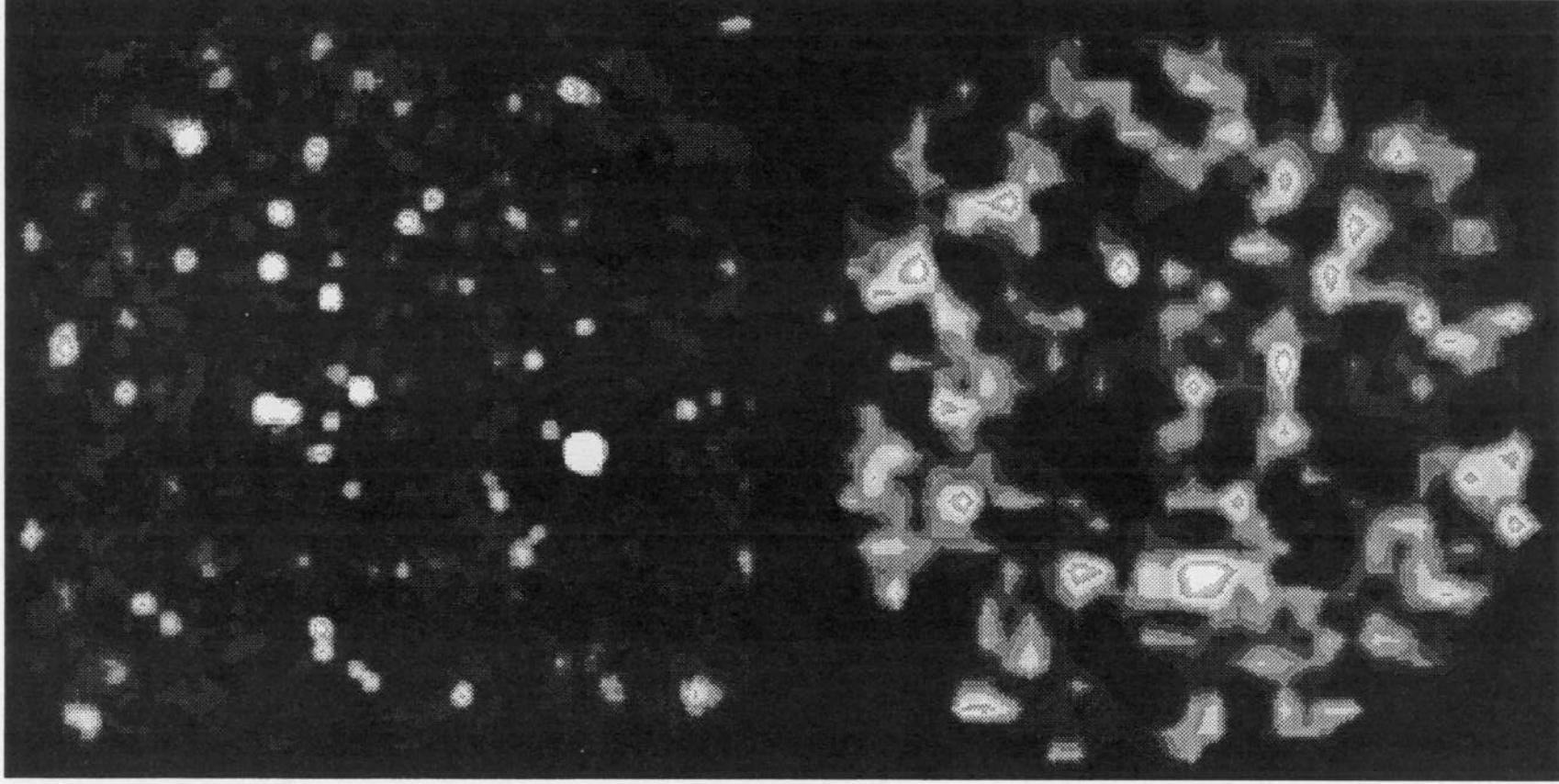
**Figure 2.** The central region of the deep survey field in the 0.4–2.4 keV band before (top panel) and after (bottom panel) removing sources brighter than ~ $0.5 \times 10^{-14}$ erg cm$^{-2}$ s$^{-1}$; the same corrections have been applied as described in Fig. 1. The size of each image is $32 \times 32$ arcmin$^2$; the pixel size in the upper panel is $15 \times 15$ arcsec$^2$ and in the bottom $1 \times 1$ arcmin$^2$, which are the same image data as for the calculations in Sections 3.1 and 3.2.

### 2.3   Removal of the non-extragalactic backgrounds

During an observation with the PSPC, events due to cosmic-ray particles and the SSX component contribute to the master veto rate (Snowden et al. 1992; Plucinsky et al. 1993) and the accepted event rate (the EE_AXE rate), respectively. The SSX signal varies around the 96-min orbit of *ROSAT*, as is evident from the periodic variation in the EE_AXE rate; additionally, other contaminations (except the Galactic one) can be traced by their temporal behaviours (see Snowden et al. 1993a for discussions). We have screened the contaminated data by flattening the light curve of the accepted rate and rejecting data with a mean master veto rate > 170. In this way 4–10 per cent of the data were rejected from the DS field and three of the MS fields (Fields 1, 3 and 4), with the result that the hard (0.4–2.4 keV) count rate away from obvious sources was statistically the same in each field. Between 15 and 20 per cent of the data were rejected from Fields 2, 5 and 6, leaving count rates that were between 30 and 100 per cent higher than for the other fields. The variation of the count rate between the separate fields due to the above contaminations is shown clearly in Fig. 3(c) (the thick line). Since the spatial distribution of all the vignetted backgrounds has no identifiable feature, the true value of the extragalactic XRB, $R_{XRB}$, can only be determined from spectral fitting after the obvious X-ray point sources have been removed from each field.

### 2.4   Removal of discrete sources

Source removal has been carried out in two ways: the first applies to the central 17-arcmin radius where the PSF of the mirror/detector combination is reasonably uniform, and the second to larger radii, particularly beyond the circular rib, where the PSF rapidly increases with radius (to an annular shape of diameter about 4 arcmin). The PSF (adapted from the XRTLIB subroutine in the Starlink ASTERIX package) is (poorly) approximated by a Gaussian with a dispersion varying with the off-axis angle $\theta$ and energy $E$ ($E$ is taken to be 1 keV). At $\theta = 0$, the dispersion is ~ 10.2 arcsec, which is consistent with the approximation from the results of Hasinger et al. 1992 (also Barcons et al. 1994).

Removal of obvious sources (brighter than a flux $S$ in erg cm$^{-2}$ s$^{-1}$) is accomplished by using sliding detection cells with different size $A$, scanning over the entire image, and masking all the pixels in the detection box from any scan in which the accumulated count rate is above the threshold

$$T_{i,j} = R_{BG}^{i,j} A + \alpha^{-1} F(\theta, A) \, SV_{\theta},\qquad(3)$$

where $i, j$ are the image coordinates in which the cell's centre is located, $\alpha$ is the conversion factor of PSPC count rate to flux (Section 2.1), $V_\theta$ is the vignetting function, $F(\theta, A)$ is the fraction of the source flux covered in the detection cell $A$, and $\theta$ is the off-axis angle of the cell to the image centre; the value of $F(\theta, A)$ is estimated from the PSF. An image in which the ribs are already masked is first processed by estimating $R_{BG}^{i,j}$ from the local background of an annulus around the detection box beyond where the source flux in the cell (if the source exists) can affect the count rate significantly. The second scan involves replacing $R_{BG}^{i,j}$ by the median count rate of the previous result (in which most obvious sources have been removed) as a global background

to remove extended sources. The flux levels and the cell size $A$ at different $\theta$ have been chosen so that the signal-to-noise ratio (S/N) of detecting the source is at least $3\sigma$ and the S/N of the XRB to the remaining source flux is above $3\sigma$ as well.

For data from the central regions of fields (~ inner 12-arcmin radius used for the MS fields and 17-arcmin radius for the DS field) with spatial resolution $15 \times 15$ arcsec$^2$, 0.5- and 0.75-arcmin-square cells are used for the first scan, and 0.5-, 0.75- and 1-arcmin-square cells for the second scan; the source detectability threshold of the MS field is equivalent to a flux of $10^{-14}$ erg cm$^{-2}$ s$^{-1}$, and that of the DS field is equivalent to $0.5 \times 10^{-14}$ erg cm$^{-2}$ s$^{-1}$ (both are in the 0.4–2.4 keV band). Fig. 4 shows the contour maps of the central MS fields (Figs 4a–f), and the image of the DS field after processing as described above is shown in the bottom panel of Fig. 2.

The increased size of the PSF beyond the ribs means that the outer region is source-confused at flux levels of $4 \times 10^{-14}$ erg cm$^{-2}$ s$^{-1}$ (for the 4-arcmin-square bin size) so that source removal is almost impossible at lower levels, whatever the depth of exposure. Source confusion in the outer parts of the image beyond the circular rib severely complicates any fitting of the vignetting function to the radial intensity profile of the whole field and means that the residual XRB is more uncertain (see equation 6) than for the central region. (It is not possible to remove sources from the whole field above a single flux, without either leaving obvious sources near the centre or running into source confusion further out.) We obtain results from the whole fields (within 45-arcmin radius) at spatial resolution $1 \times 1$ arcmin$^2$, by using 2- and 3-arcmin-square cells for both source-searching scans, and masking pixels containing sources brighter than $5 \times 10^{-14}$ and $3 \times 10^{-14}$ erg cm$^{-2}$ s$^{-1}$ for the MS and DS fields, respectively. The final merged strip of the MS fields without bright sources is shown in the right panel of Fig. 1.

### 2.5   Spectral fitting

Spectra have been extracted in pulse-height-analyser (pha) channels appropriate to the energy band 0.2–2.4 keV from source-free regions within the central 12-arcmin radius of each field (Fig. 3d). Following the calibrations of Snowden et al. (1992) and Plucinsky et al. (1993), we have subtracted the residual particle spectra from the raw data of each field and modelled the whole band spectrum with the following components (Hasinger 1992; Wang & McCray 1993): a power-law spectrum for the extragalactic XRB, two hot thermal plasma (Raymond & Smith 1977) components to characterize the halo and the local bubble hot gases, and an oxygen fluorescent line at 0.54 keV to represent the residual SXX (Snowden & Freyberg 1993). The Galactic column density is assumed for the absorption of the power-law component, while the absorption of the halo gas is left as a free parameter.

Although the high quality of the PSPC data gives us the capability to solve such a complicated model, lack of knowledge of the spatial variations in the Galactic XRB (temperature and flux) on scales less than a few degrees results in the involvement of more free parameters. Without any further constraint, the individual fitting of each field gives a generally unacceptable result of the photon index of the XRB (from 1.02 to 1.6). It is a first-order approximation to define the
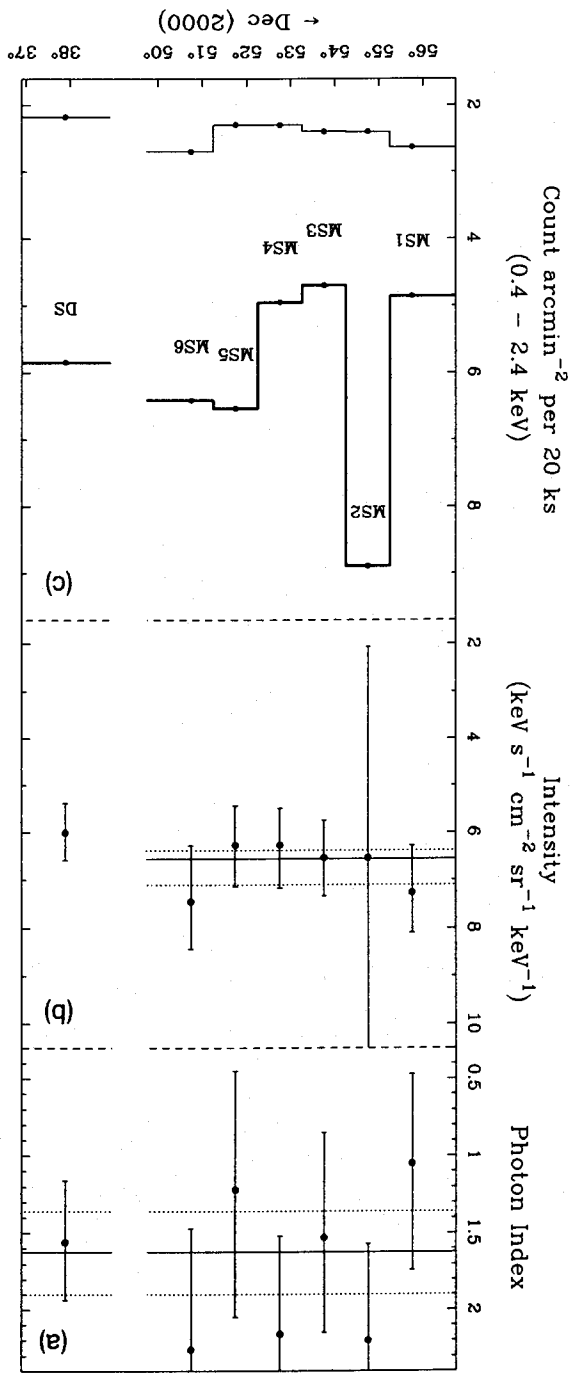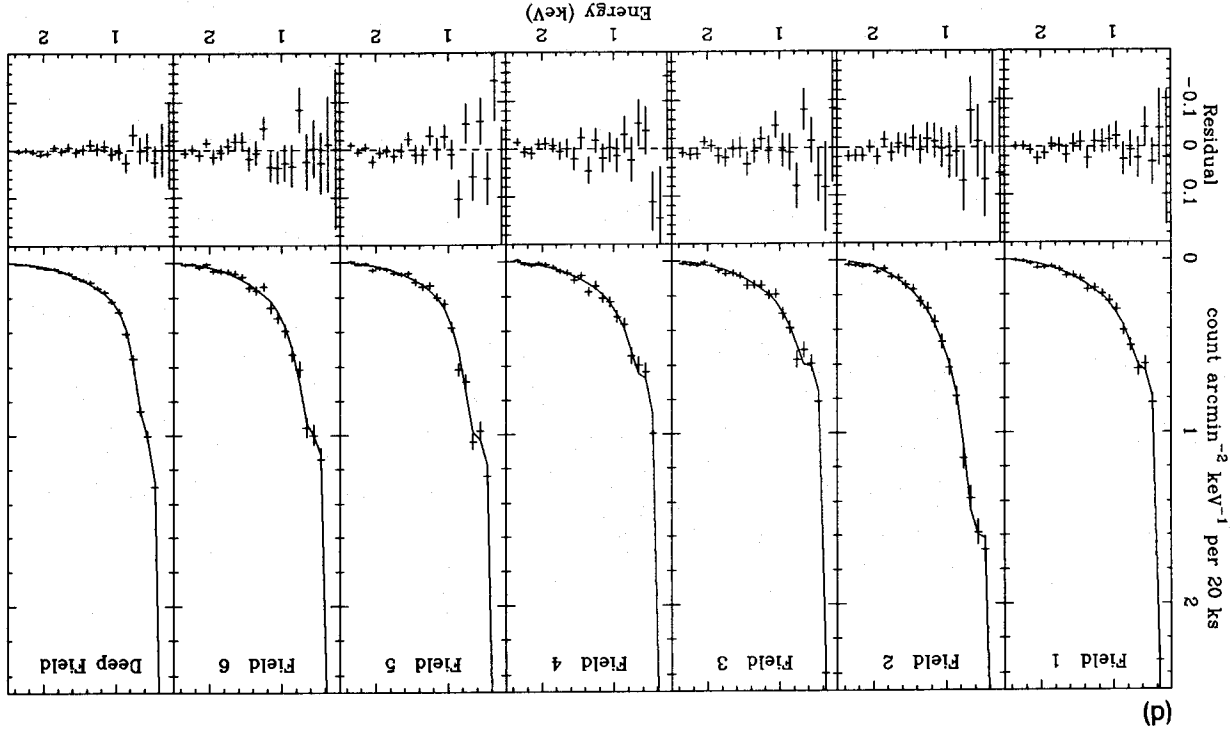
**Figure 3.** (a) The best-fitting value of the power-law photon index (the horizontal solid line) and its 90 per cent confidence intervals (dotted lines) from the combined spectral fitting (to the three-component model) of the DS and five MS fields in the 0.2–2.4 keV range; scattering point data are the best-fitting values for each field to the same model (fixing the temperature of the local bubble at $10^6$ K and the absorptions) individually. The x-axis is the Dec. coordinate, and the centre of each field is indicated by a spot. (b) The best-fitting value of the normalization of the power-law component and its 90 per cent confidence intervals from the combined fitting of five MS and the DS fields in the range 0.2–2.4 keV; the horizontal solid line is the mean value of the MS fields, and its 90 per cent confidence intervals are indicated by the dotted lines. Field 2 is later fitted individually and causes a large error. (c) The observed XRB count rates (the thick line) in the 0.4–2.4 keV band within the inner 12-arcmin radius for MS fields 1 to 6 and the DS field, from left to right; the MS fields are free from discrete sources of flux above $10^{-14}$ erg cm$^{-2}$ s$^{-1}$ and the DS field is free above $0.5 \times 10^{-14}$ erg cm$^{-2}$ s$^{-1}$. No correction has been applied, except for removal of the particle background. The unevenness across the fields is due to various contaminations, mostly in the soft band (as indicated in Fig. 3d), but the count rates due to the extragalactic XRB, estimated from the power-law component of the spectral fitting, are essentially equal (the thin line). (d) The observed count spectra and the best-fitting model folded with the detector response (the solid line) for the six MS fields and the DS field (from left to right). The residual is the difference between the observed data and the model.
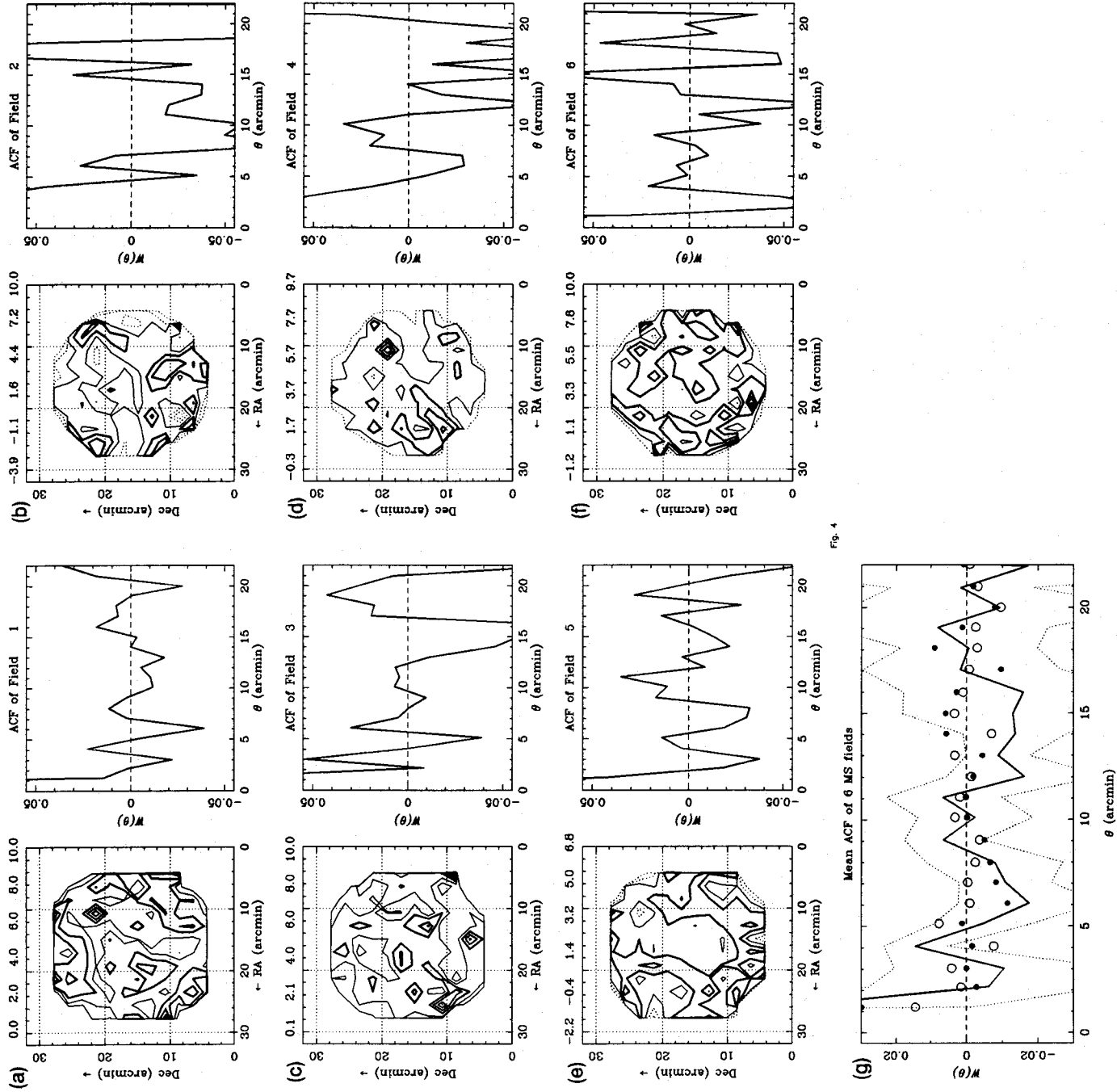
**Figure 4.** (a)–(f) The contour maps and ACF of the MS Fields 1–6 within the central ∼ 12-arcmin radius, excluding sources brighter than $10^{-14}$ erg cm$^{-2}$ s$^{-1}$ and other contaminations (from left to right and from top to bottom as marked). The intensity levels are labelled above each contour map in units of count arcmin$^{-2}$ (20 ks)$^{-1}$, the thick contours indicate levels above the mean value, the dotted contours indicate levels that are negative due to the uniform subtraction of the non-extragalactic XRB. Note that, in each image, bright sources have been removed on a finer pixel scale (15 arcsec square) than shown here, where the unit pixel is 1 arcmin square. (g) The average ACF of the six MS fields weighted by the standard deviation at each angular separation, with 2σ limits shown by the dotted lines. Filled circles are the ACF of the central DS field with pixel size = 1×1 arcmin$^2$ (the bottom panel of Fig. 2), in comparison to the ACF derived from the same image in the 0.9–2.4 keV band (open circles).

temperature of the local bubble as $10^6$ K, and a simultaneous fitting of all spectra (except Field 2 which is contaminated by a low-surface-brightness cluster, see Fig. 1) can improve the uncertainties of all the free parameters. We fit the 0.2–2.4 keV spectra to the above model with additional constraints of forcing the halo gas temperature in the MS fields and its absorption all over the sky to be uniform: the best-fitting ($\chi^2$/d.o.f. = 111.7/112) value of the photon index is 1.6 with a 90 per cent confidence interval of [1.31, 1.85] (Fig. 3a), and the normalization of the intensity of each field varies slightly

(Fig. 3b), with mean values of 6.56 [6.38, 7.1] and 6.0 [5.38, 6.59] for the MS and DS fields, respectively. The Galactic flux has stronger fluctuations in the sky than the extragalactic XRB, demonstrating the large-scale spectral variability of the Galactic XRB even at high Galactic latitude (see McCammon & Sanders 1990). The best-fitting values of the halo gas temperature are 0.16 [0.147, 0.167] and 0.137 [0.115, 0.14] keV for the MS and DS fields, respectively, with an absorption $= 3.6 \times 10^{19}$ cm$^{-2}$. The spectrum of Field 2 was later fitted to the same model with an additional cluster model component and the best-fitting values derived. The spectra and their best fits of the MS and DS fields are shown in Fig. 3(d), and the total XRB count rate of each field is indicated by the thick line in Fig. 3(c).

As most results of the spectral fitting (e.g. Hasinger 1992; Wang & McCray 1993) show the Galactic emission above 1.1 keV to be insignificant, we fit the 1.1–2.4 keV spectra only to a simple power-law model, and the result is consistent with that of the whole-band fitting; the best-fitting ($\chi^2$/d.o.f.$=64.15/82$) value of the photon index is 1.626 [1.36, 1.9], and the mean normalizations are 7.09 [6.75, 7.43] and 6.12 [5.53, 6.74] for the MS and DS fields, respectively.

The results from the spectral fitting imply that the fluxes of the extragalactic XRB rate in the range 0.4–2.4 keV containing point sources of fluxes $S_m$ less than $10^{-14}$ and $0.5 \times 10^{-14}$ erg cm$^{-2}$ s$^{-1}$ are 11.9 and 10.9 keV cm$^{-2}$ s$^{-1}$, respectively, which are lower than previous estimates (Table 1) obtained from other instruments (the best-measured XRB fluxes before *ROSAT* may contain more contamination and unresolved discrete sources of higher flux). The count rate of the power-law component in each field is calculated (the thin line in Fig. 3c), and later applied to the ACF calculation. The mean conversion factor is 1 PSPC count s$^{-1}$ (0.4–2.4 keV) $= 1.4 \times 10^{-11}$ erg cm$^{-2}$ s$^{-1}$. Finally, we note, on using the *ROSAT* log $N$–log $S$ curve (Hasinger et al. 1993), that the XRB flux could be saturated by integrating down the source counts at a flux level $\sim 4 \times 10^{-16}$ erg cm$^{-2}$ s$^{-1}$ in the same energy band.

It is not yet clear that the extragalactic XRB component should be assumed to be solely a power law (soft excesses are seen in AGN and there could be other soft sources), while some of the halo contributions could be extragalactic (Snowden et al. 1993b). Nevertheless, we proceed by using the power-law component alone, and hereafter define that to be the XRB.

# 3 THE RESULTS

## 3.1 The ACF

Due to variations in the uncertainty of the data from pixel to pixel, the ACF defined in equation (1) is modified to

$$W(\theta) = \frac{\sum\sum (I_{i,j} - \bar{I})(I_{i',j'} - \bar{I})(\omega_{i,j}\omega_{i',j'})^{1/2}}{\bar{I}^2 \sum\sum(\omega_{i,j}\omega_{i',j'})^{1/2}}. \tag{4}$$

The weighting factor $\omega_{i,j} = t_{\exp} V_{i,j}/t_N$, where $t_{\exp}$ and $t_N$ are the exposure time and the normalization time (20 ks), $V_{i,j}$ is the vignetting function, and the subscripts $i$, $j$ and $i'$, $j'$ correspond to the position of the pixels in the image. $\bar{I}$ is the mean intensity in the (masked) fields, which corresponds to the count rate of the power-law component derived in Sec-

tion 2.5. The $\omega_{i,j}$ value of bad or missing data (covered by the window-support structure or bright point sources) is set to 0. We have calculated the ACF using the best available data for each angular scale. The particle background has been first subtracted from each source-free field according to the formulae of Plucinsky et al. (1993), followed by a uniform subtraction to make the median of each field equal to the predicted XRB count rate from the spectral fitting (the thin line in Fig. 3c). For data within the inner 45-arcmin radius, the extra flux contributed from the discrete sources of flux from 1 to $5 \times 10^{-14}$ erg cm$^{-2}$ s$^{-1}$ is estimated from the integration of the XRB log $N$–log $S$ curve (Hasinger et al. 1993), which is $\sim 9.95$ keV cm$^{-2}$ s$^{-1}$ sr$^{-1}$. For scales below $\sim 30$ arcmin with a spatial resolution $\sim 1$ arcmin, we have used the central regions of each of the MS (Figs 4a–f) and DS (filled circles in Fig. 4g obtained from the image data in the bottom panel of Fig. 2) fields, and have formed an average ACF of the MS fields (Fig. 4g) by using the weighted mean of the results from the individual ACFs (Figs 4a–f). The ACFs from either the central DS or the average MS fields (Fig. 4g) show no obvious structure on small scales, apart from the relatively strong correlation at 1 arcmin, which is consistent with that expected from the flux remaining from bright sources after excising the pixels above threshold (Section 2.4). A marginally significant ($\sim 2\sigma$) anticorrelation is apparent around scales of 6–8 arcmin.

For a final large-scale ACF calculation up to $\sim 5°$, we have merged the six MS fields within 45-arcmin radius by matching them at the regions of overlap after each field has been normalized in exposure time by division by the ratio of the exposure time to 20 ks. The ACF of the MS merged strip with a pixel size $4 \times 4$ arcmin$^2$ (the same image data in the right panel of Fig. 1) is shown in Fig. 5(a) (filled circles). Combining results from the MS merged strip and the central DS field as shown in Fig. 5(a), we have obtained the weighted ACF over angular scales from 1 arcmin to 5°, which covers the range of most previous work on the ACF. Fig. 5(b) also shows the comparison with previous upper limits [on an updated version of fig. 6 from Fabian & Barcons (1992) (Barcons, private communication)]. Since the ACF is subject to the mean value of the XRB count rate and we have used a significantly low value determined from the spectral fitting, the upper limit of our result is generally above previous ones. After correction for the Poisson term of the ACF (estimated from the mean of simulations, see Carrera et al. 1993), the ACF of the DS field from 2–17 arcmin is below $2 \times 10^{-2}$ at 95 per cent confidence, and on larger angular scales our ACF results are above the *Ginga* results. Following the processes as described above, a similar result is obtained from the image of the central DS field in the range 0.9–2.4 keV (open circles in Fig. 4g), in which neither the Galactic nor the SSX has a significant effect.
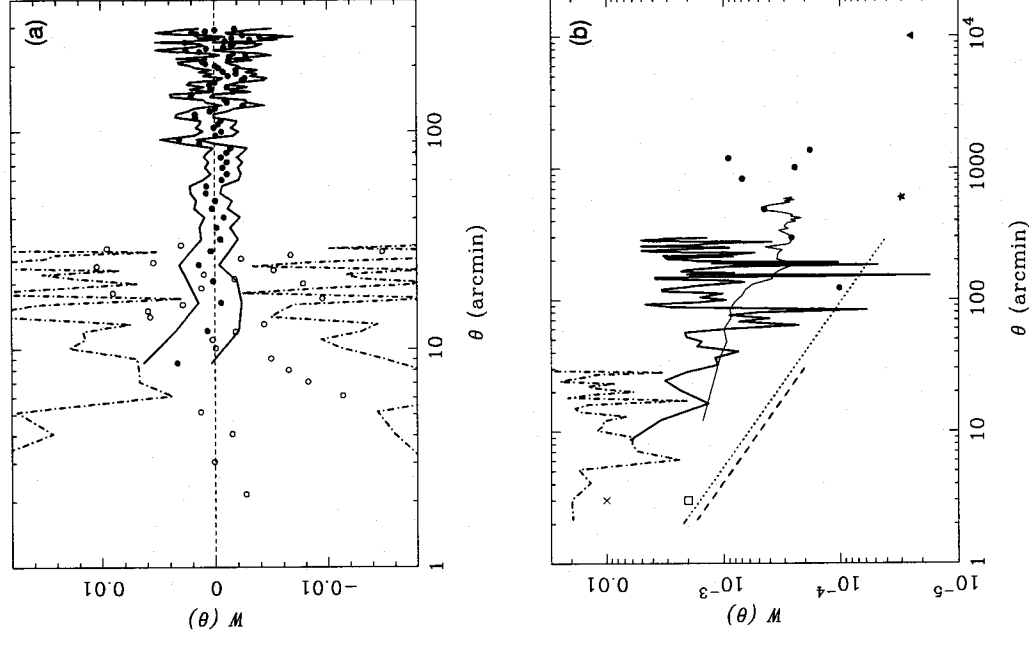
In spite of the relatively higher upper limit, the collective behaviour of the ACF from arcmin to degree scales is consistently flat when taking the uncertainty of each data point into account; furthermore, a weighted fitting to a power-law $W(\theta) = \alpha\theta^{-0.8}$ model (derived in Section 4) reduces the upper limit immediately (the error in $\alpha$ is estimated by simulations). The best fit of the 2–30 arcmin ACF data gives $\alpha = (-4.86 \pm 3.98) \times 10^{-3}$ and, with constraints from the larger scale, $\alpha = (0.50 \pm 1.68) \times 10^{-3}$ is obtained from the combined fitting of the DS and MS data for 2–300 arcmin

(Fig. 5a). During each fitting, data that could be contaminated by the PSF have been excluded.

## 3.2  Excess fluctuations

The intensity fluctuations of the sky brightness as a function of angular scale have been obtained by taking independent bins of increasing scale size and determining

$$\frac{\delta I}{I} = \sqrt{\frac{\sum (I_{i,j} - \bar{I})^2 \, \omega_{i,j} N}{\bar{I}^2 \sum \omega_{i,j} (N-1)}},$$  (5)

which is identical to $W^{1/2}(\theta=0)$, and where $N$ is the number of pixels used. We have obtained strong limits on $\delta I/I$ over scales of 1 arcmin–2° (Fig 6), using the central regions of the DS field and the regions beyond the ribs from the merged strip as for the ACF.

The excess fluctuations are obtained by subtracting the confusion noise and Poisson noise. The Poisson noise is intrinsically imprinted by the original input count rate and then rescaled by the vignetting factor and normalization time-scale (i.e. proportional to the weighting factor) for each pixel. The confusion noise is due to unresolved sources fainter than $S_m$ defined as (e.g. Barcons et al. 1994)
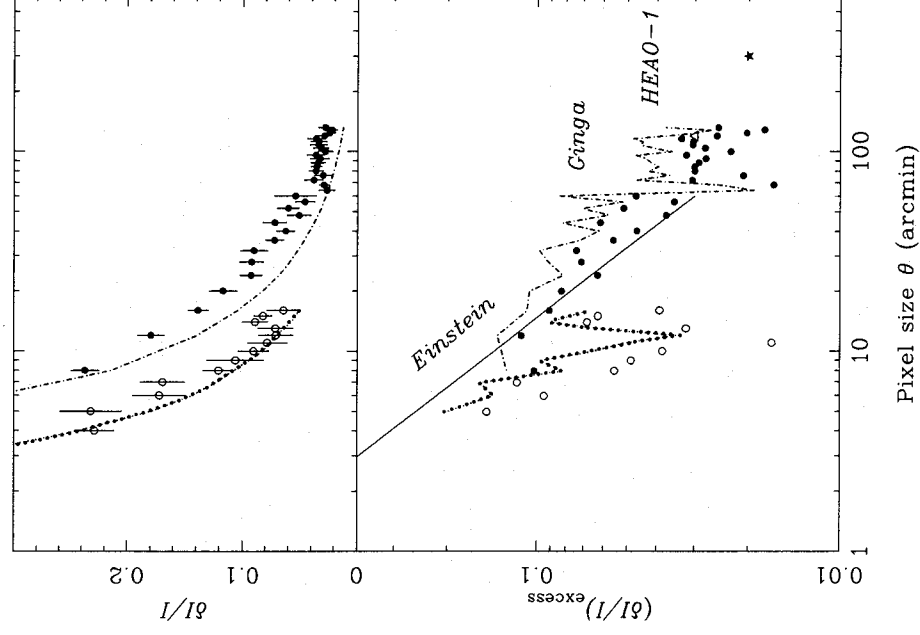


**Figure 5.** The combined ACF result from the MS merged strip and the central DS field. (a) Open circles are the ACF of the central DS field in the 0.4–2.4 keV band from Fig. 4(g); filled circles are for the MS merged strip with pixel size = 4×4 arcmin² (the right panel of Fig. 1). After correction for the Poisson term, the 95 per cent confidence intervals are estimated from the reshuffling simulations (method 2) and indicated by the thick dot-dashed and solid lines, respectively, for the central DS and MS merged strip. (b) 2σ upper limits of ACFs from the central DS and MS merged strip are denoted by the thick dot-dashed and solid lines, respectively. The 95 per cent upper limits of the best-fitting curves of the DS and DS+MS data are the thick dashed and dotted lines respectively. The square at $\theta=3$ arcmin is the upper limit obtained from *Einstein* Observatory data (Soltan 1991), the cross at the same scale is from earlier *ROSAT* data (Hasinger 1992), the thin solid line and filled circles are from *Ginga* scans and pointed data, respectively (Carrera et al. 1991, 1993), the filled star is from *HEAO-1 A2* data, and the filled triangle is the dipole from Shafer (1983).



**Figure 6.** The combined $\delta I/I$ result from the MS merged strip and the central DS field. Upper panel: the dotted and dot-dashed lines are the predicted fluctuations due to the Poisson and confusion noise, $(\sigma_{Poisson}^2 + \sigma_{confusion}^2)^{1/2}/I$, open circles stand for the $\delta I/I$ of the DS field, filled circles for the MS merged strip. The error bars are derived from the standard deviations (method 1). Bottom panel: the excess fluctuations of the DS field (open circles) and MS merged strip (filled circles). The dotted and dot-dashed lines represent the $2\sigma$ upper limits. The solid line is the upper limit from the $P(D)$ analysis using the *Einstein* Observatory data. The triangle at ~100 arcmin and filled star are the results from *Ginga* and *HEAO-1* data, respectively.

$$\sigma^2 = K\Omega_{\text{eff}} S_B^{\gamma-1} \frac{S_m^{3-\gamma}}{3-\gamma}, \qquad (S_m < S_B), \tag{6}$$

$$\sigma^2 = K\Omega_{\text{eff}} \left[ S_B^2 \left( \frac{1}{3-\gamma} - 2 \right) + 2S_B^{3/2} S_m^{1/2} \right], \qquad (S_m > S_B), \tag{7}$$

where $\Omega_{\text{eff}}$ is the effective area defined (Condon 1974) as $\int [f(\theta, \phi)]^{\gamma-1} \, d\Omega$; $f(\theta, \phi)$ is the detector response profile (given by the convolution of the PSF with the pixel), $S_B$, $\gamma$ and $K$ are from the model of the log $N$–log $S$ of the source population, which is assumed to be a broken power law (Barcons et al. 1994; Hasinger et al. 1993)

$$n(S) = \frac{K}{S_B} \left( \frac{S}{S_B} \right)^{-\gamma}. \tag{8}$$

When the source flux $S > S_B$, the slope is approximately the Euclidean case, namely $\gamma = 2.5$; however, for fluxes below $S_B$, the slope of log $N$ – log $S$ is observed to be flatter, which reflects the cosmological effect. We use $S_B = 2.52 \times 10^{-14}$ erg cm$^{-2}$ s$^{-1}$, $K = 109$ deg$^{-2}$, and $\gamma = 1.72$ from Hasinger et al. 1993 (see also Barcons et al. 1994 for a consistent result), and $\Omega_{\text{eff}}$ is approximated by the binned pixel size throughout this work.

Our results show $\delta I/I$ to be dominated by confusion noise. As shown in Fig. 6, the observed fluctuation is comparable to the quadratic sum of the Poisson and confusion noise in $2\sigma$. The observed $\delta I/I$ and $(\sigma_{\text{Poisson}}^2 + \sigma_{\text{confusion}}^2)^{1/2}/I$ are shown in the upper panel of Fig. 6. A strong constraint on the excess fluctuation of <20 per cent down to a few-arcmin scale is found at 95 per cent confidence (bottom panel). This confirms that the $P(D)$ distribution is not contaminated by any large-scale effects, such as source clustering etc.

### 3.3 Estimate of confidence intervals

The confidence intervals for the ACF and $\delta I/I$ have been estimated in two ways. The first is by calculating the standard deviations of $W(\theta)$ and $\delta I/I$ at each angular scale (Persic et al. 1991). For the ACF, the standard deviation $\sigma_\theta$ of $\langle \delta I \delta I_\theta \rangle / \langle I \rangle^2$ contributed from $N_\theta$ pairs of pixels separated by $\theta$ is calculated, and the error in the mean, namely $W(\theta)$, is therefore $\sigma_\theta / \sqrt{N_\theta}$. For $\delta I/I$, we calculate the standard deviation $\sigma_{\text{ms}}$ of $(\delta I/I)^2$ as above, and the error $\sigma_{\text{rms}}$ of $\delta I/I$ is related to $\sigma_{\text{ms}}$ by $\sigma_{\text{rms}} = \sigma_{\text{ms}}(2\delta I/I)^{-1}$.

The second method involves reshuffling the positions of pixels with a non-zero weighting factor. After generating 300 pseudo-samples, we calculate the ACFs and $\delta I/I$ of each sample; the standard deviation of the values from these simulations then provides an estimate of the confidence interval. Both methods give consistent results for the ACF, whereas the error bar derived from the reshuffling method is generally larger than the other by a factor of up to 2 for the $\delta I/I$ fluctuations. Throughout this work the upper limits are determined from method 2 for $W(\theta)$ because it takes into account the correlation of the data, and from method 1 for $\delta I/I$ because it can be derived analytically.

To estimate the uncertainty of the best-fitting $\alpha$ of the observed ACF (see Section 3.1), we have performed exactly the same fitting to the ACF of the pseudo-samples, and

derived the standard deviation of the 300 best fits as the uncertainty of $\alpha$ (for a similar case, see the discussion by Barcons & Fabian 1989).

## 4 INTERPRETATION OF RESULTS

Since the faint sources constituting the residual XRB cannot yet be identified directly with any known astronomical objects, we must attempt to constrain the physical properties of these objects indirectly. The above results of the ACF and excess fluctuation analyses can strictly constrain the possible candidates for the XRB by defining their spatial distribution. We will discuss the implications from the excess fluctuation for cosmological diffuse sources in another paper (Chen & Fabian, in preparation). Here we will concentrate on the ACF results. The observed ACF, which provides information on source clustering, has been applied to models of known X-ray sources by several authors (e.g. Barcons & Fabian 1989; Carrera et al. 1991, and upper limits of the contribution of each to the XRB are obtained. Instead of checking each known X-ray source class (e.g. AGNs, starburst galaxies, galaxy clusters...), we will investigate the constraints on the clustering size of any possible sources from a more general approach. Constants with cosmological interest are set to the generally accepted values, i.e. $\Lambda = 0$, $\Omega = 1$, $q_0 = 0.5$ and $H_0 = 50\ h_{50}$ km s$^{-1}$ Mpc$^{-1}$, with $h_{50} = 1$.

The clustering of sources is described by the spatial correlation function $\xi(z, r)$ which is modelled by a power law (Peebles 1980; Bahcall & Soneira 1983),

$$\xi(z, r) = (1+z)^{-3-\epsilon} \left( \frac{r}{r_0} \right)^{-\gamma}, \tag{9}$$

where $r_0$ characterizes the spatial scale of the cluster in the *proper* coordinate, $\epsilon$ indicates how the cluster evolves: positive and negative values of $\epsilon$ represent, respectively, growing and decaying clustering with cosmic time, while $\epsilon = 0$ implies stable clustering. Evolution due only to the expansion of the Universe leads to $\epsilon = \gamma - 3$, and linear growth of fluctuations to $\epsilon = \gamma - 1$; $\epsilon = -3$ means no evolution physically. The observed intensity of sources in an effective area $\Omega_{\text{eff}}$ of the detector is

$$
\begin{aligned}
\langle I_{\text{source}} \rangle &= \frac{c\Omega_{\text{eff}}}{4\pi H_0} \int d(\log L)\, L(z) \int_{z_{\text{min}}}^{z_{\text{max}}} dz\, K(L, z)\, n(L, z)(1+z)^{-5.5},
\end{aligned}
\tag{10}
$$

where $K(L, z)$ is the $K$-correction factor, $n(L, z) = (1+z)^3 n_0(L, z)$ is the number density of sources and $n_0(L, z)$ is the present-day number density. With the effective volume emissivity defined by

$$j_{\text{eff}}(z) = \int d(\log L)\, L(z)\, K(L, z)\, n_0(L, z),$$

equation (10) becomes

$$\langle I_{\text{source}} \rangle = \frac{c\Omega_{\text{eff}}}{4\pi H_0} \int_{z_{\text{min}}}^{z_{\text{max}}} j_{\text{eff}}(z)(1+z)^{-2.5}\, dz.$$

With the assumption that the correlation length $r_0$ of the source is much smaller than the distance of the source to the

observer, the theoretical angular ACF of the sources $w(\theta)$ is related to the spatial correlation function by (e.g De Zotti et al. 1990; Martin-Mirones et al. 1991)

$$w(\theta) = \left(\frac{c\Omega_{eff}}{4\pi H_0}\right)^2 \frac{\int_{z_{min}}^{z_{max}} dz\, j_{eff}(z)^2 (1+z)^{-5} \int d(\delta z)\, \xi(r,z)}{\langle I_{source}\rangle^2}, \quad (11)$$

where $\theta$ is the angular separation of any two patches (with an effective area $\Omega_{eff}$) in the sky. The analytical solution of the integration of the spatial correlation function $\xi(z, r)$ gives (Totsuji & Kihara 1969)

$$\int \xi(r, z)\, d(\delta z) = -\frac{\Gamma\left(\frac{1}{2}\right)\Gamma\left(\frac{\gamma - 1}{2}\right)}{\Gamma\left(\frac{\gamma}{2}\right)}$$

$$\times \left(\frac{H_0}{c} r_0\right)^\gamma (2\theta)^{1-\gamma}(1+z)^{-\epsilon+\gamma-1.5}[1-(1+z)^{-1/2}]^{1-\gamma},$$

where $\Gamma$ denotes the gamma function; for $\gamma = 1.8$ and assuming $j_{eff}(z)$ during the X-ray emission epoch $(z_{min}, z_{max})$ to be constant, equation (11) is reduced to

$$w(\theta) = 5.1 \times 10^{-4} r_{0\,Mpc}^{1.8} \theta_{1'}^{-0.8} \phi(z_{min}, z_{max}, \epsilon), \quad (12)$$

where $\phi(z_{min}, z_{max}, \epsilon)$ is the coefficient representing the net cosmological effect,

$$\phi(z_{min}, z_{max}, \epsilon) = \frac{\int_{z_{min}}^{z_{max}} (1+z)^{-\epsilon+\gamma-6.5}[1-(1+z)^{-1/2}]^{1-\gamma}\, dz}{[(1+z)^{-1.5} \Big|_{z_{max}}^{z_{min}}]^2}. \quad (13)$$

The constraint from the observed ACF is $W(\theta) \geq (\langle I_{source}\rangle / \langle I_{XRB}\rangle)^2 w(\theta) = f^2 w(\theta)$, where $f$ is the fraction of sources contributing to the observed XRB; the upper limits of both $f$ and correlation length $r_0$ are constrained by

$$r_{0\,Mpc} f^{10/9} \leq [1.96 \times 10^3 W(\theta) \theta_{1'}^{0.8} \phi(z_{min}, z_{max}, \epsilon)^{-1}]^{5/9}. \quad (14)$$

Applying the 95 per cent upper limit from the fitting of the ACF over 2–300 arcmin, $W(\theta) \theta_{1'}^{0.8} = 3.86 \times 10^{-3}$ for the case of $\epsilon = 0$, $-1.2$, $-1.8$ and $-3$, we have calculated the
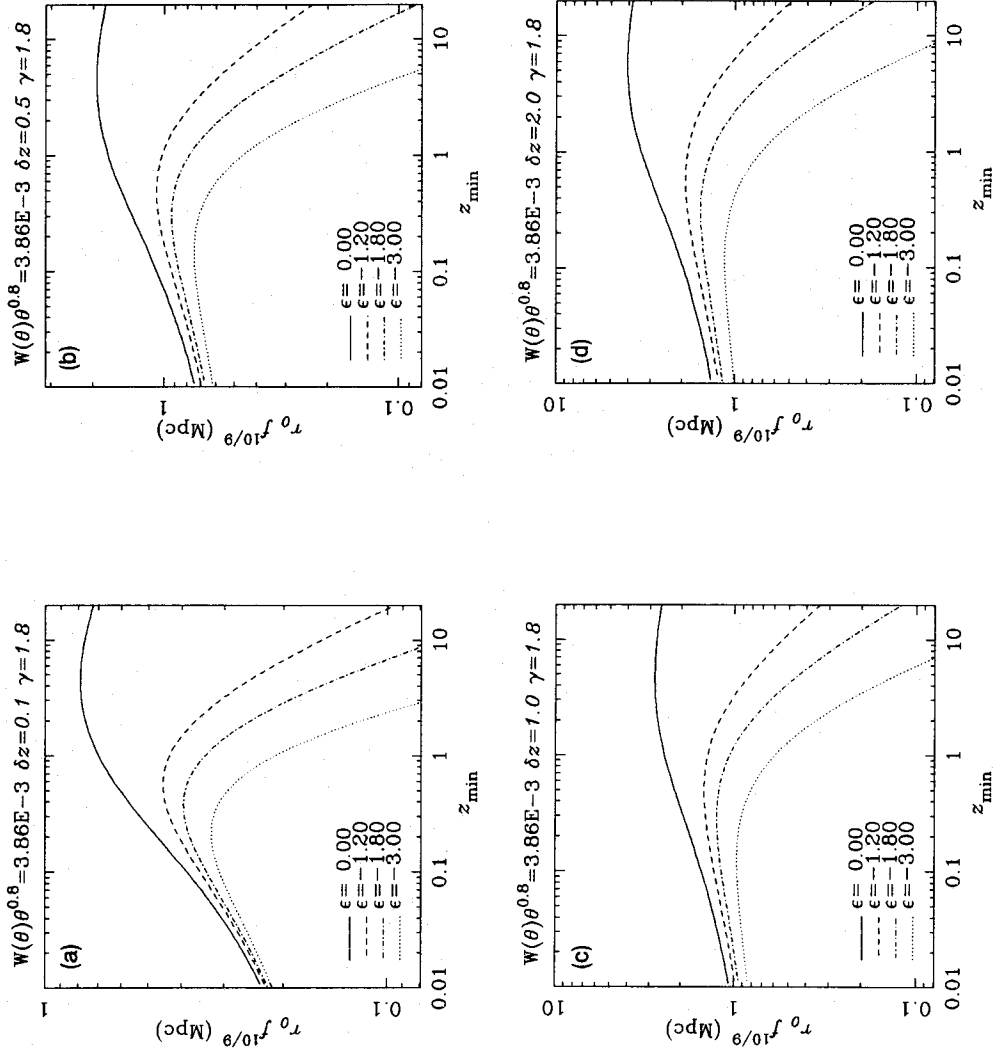


**Figure 7.** $r_0 f^{10/9}$ plotted against $z_{min}$, based on equation (14) – the upper limit of the contribution from sources, in the epoch $(z_{min}, z_{min} + \delta z)$ and with correlation length $r_0$, to the residual 0.4–2.4 keV XRB, where the power-law index $\gamma$ of the spatial correlation function is $-1.8$. The solid line is for stable clustering evolution $(\epsilon = 0)$, the dashed line for comoving clustering $(\epsilon = -1.2)$, the dot-dashed line for linear growth of fluctuation $(\epsilon = -3)$, and the dotted line for physical unchanging clustering $(\epsilon = -1.8)$. $\delta z$ is equal to 0.1, 0.5, 1 and 2 in Figs 7(a)–(d).

**Table 1.** Estimates of the XRB.

| Model | $S_m$ (erg cm$^{-2}$ s$^{-1}$) | Predicted flux (0.4–2.4 keV) (keV cm$^{-2}$ s$^{-1}$ sr$^{-1}$) | Reference |
|---|---|---|---|
| $6.56E^{-0.6}$ | $10^{-14}$ | 11.9 | This work |
| $6.0E^{-0.6}$ | $0.5 \times 10^{-14}$ | 10.9 | This work |
| $6.6E^{-1.1*}$ | $\sim 10^{-14}$ | 11.9 | Hasinger 1992 |
| $9.5E^{-0.7}$ | $10^{-14}$ | 17.12 | Wang & McCray 1993 |
| $15E^{-0.7}$ | $4 \times 10^{-14}$ | 27 | Wu et al.1991 |
| $11E^{-0.4}$ | | 20.47 | McCammon & Sanders 1990 |

*After subtracting the mean source spectrum from the total spectrum.

constraint on $f$ and $r_0$ for $z_{min} \in [0.01, 20]$ with a fixed interval $\delta z = 0.1, 0.5, 1$ and 2 (see Figs 7a–d). It is shown that a greater contribution from a given source class can be allowed (where $r_0$ is fixed) when the clustering evolution is stable, i.e. $\epsilon = 0$. The contribution from each epoch is estimated when $\delta z \to 0$, and the redshift at which $r_0$ peaks is found to be around 1. If the residual XRB originates from $z_{max} \lesssim 1$ (e.g. Figs 7a–c), then $r_0 \lesssim 2\ h_{50}^{-1}$ Mpc (the higher $z$ constraint relies on the correlation function extending as a power law to large scales), and generally $r_0 \lesssim 4\ h_{50}^{-1}$ Mpc (Fig. 7d).

## 5 CONCLUSION

Our constraints on the observed ACF and the excess fluctuations from analysis of the MS and DS fields supersede previous work on some scales (Figs 5 and 6), although it must be noted that many of the other results are from different (harder) energy bands and, when in the soft band, use different estimates of the diffuse extragalactic XRB flux. We have measured a low $2\sigma$ upper limit of 0.2 on $\langle \delta I/I \rangle_{excess}$ above a few-arcmin scale, and the excess fluctuations above this scale show consistency with the results from the *Einstein* Observatory data. The ACF of each individual MS central field (Figs 4a–f) is noisy, probably due to the remaining faint sources below the detection threshold, but gives an average weighted ACF (Fig. 4g) which is relatively smooth and consistent with the ACF of the central DS. With a pixel size of $4 \times 4$ arcmin$^2$, the merged strip of MS fields is flat from scales of a few arcmin to degrees. We do not obtain values on degree scales as low as the *Ginga* data of harder energy (Carrera et al. 1991), but the further *ROSAT* PSPC extended Deep Survey may improve on it if it is due to the underlying faint sources. Alternatively, it may be another symptom of the different energy bands [recall the similar case of the $P(D)$ analysis, e.g. Fabian & Barcons (1992)]. From the spectral fitting, we find that the power-law component of the XRB count rate is lower than most previous estimates (Table 1) by a factor of a few. As a result of a low intensity, the upper limit of the ACF is higher than that expected, but the result from the combined, weighted ACF improves on the upper limits from the data reported earlier from the same instrument (Hasinger et al. 1991; Carrera & Barcons 1992; Hasinger 1992), and stricter constraints have been found over the scale of 2 arcmin–5°.

For most cases of the evolution parameter $\epsilon$, our best limit to the ACF implies that the residual soft XRB cannot originate from large-scale structure with a correlation length $r_0 > 4\ h_{50}^{-1}$ Mpc from any possible redshift, which is below the typical clustering scale of AGNs ($\sim 12\ h_{50}^{-1}$ Mpc, e.g.

Boyle et al. 1991) and galaxy clusters ($\sim 50\ h_{50}^{-1}$ Mpc, e.g. Bahcall & Soneira 1983). The residual soft XRB, after removal of obvious sources, appears to be very smooth and less than 50 per cent of it can originate from sources clustered more strongly than normal galaxies ($\sim 11\ h_{50}^{-1}$ Mpc, e.g. Davis & Peebles 1983).

## REFERENCES

Bahcall N. A., Soneira R. M., 1983, ApJ, 270, 20
Barcons X., Fabian A. C., 1989, MNRAS, 237, 119
Barcons X., Branduardi-Raymont G., Warwick R. S., Fabian A. C., Mason K. O., McHardy I., Rowan-Robinson M., 1994, MNRAS, in press
Boyle B. J., Jones L. R., Shanks T., Marano B., Zitelli V., Zamorani G., 1991, in Crampton D., ed., ASP Conf. Ser. Vol. 21, Space Distribution of Quasars. Astron. Soc. Pac., San Francisco, p. 191
Branduardi-Raymont G. et al., 1994, MNRAS, submitted
Butcher J. A. et al., 1994, MNRAS, submitted
Carrera F. J., Barcons X., 1992, MNRAS, 257, 507
Carrera F. J., Barcons X., Butcher J. A., Fabian A. C., Stewart G. C., Warwick R. S., Hayashida K., Kii T., 1991, MNRAS, 249, 698
Carrera F. J. et al., 1993, MNRAS, 260, 376
Condon J. J., 1974, ApJ, 188, 279
Davis M., Peebles P. J. E., 1983, ApJ, 267, 465
De Zotti G., Persic M., Franceschini A., Danese L., Palumbo G. G. C., Boldt E. A., Marshall F. E., 1990, ApJ, 351, 22
Fabian A. C., Barcons X., 1992, ARA&A, 30, 429
Georgantopolous I., Stewart G. C., Shanks T., Griffiths R. E., Boyle B. J., 1993, MNRAS, 262, 619
Hasinger G., 1992, in Barcons X., Fabian A. C., eds, The X-ray Background, Cambridge Univ. Press, Cambridge, p. 229
Hasinger G., Schmidt M., Trümper J., 1991, A&A, 246, L2
Hasinger G., Turner J. T., George I. M., Boese G., 1992, GSFC OGIP Calibration Memo CAL/ROS/92-001
Hasinger G., Burg R., Giacconi R., Hartner G., Schmidt M., Trümper J., Zamorani G., 1993, A&A, 275, 1
McCammon D., Sanders W. T., 1990, ARA&A, 28, 657
Martín-Mirones J. M., De Zotti G., Boldt E. A., Marshall F. E., Danese L., Franceschini A., Persic M., 1991, ApJ, 379, 507
Mushotzky R. F., 1992, in Barcons X., Fabian A. C., eds, The X-ray Background. Cambridge Univ. Press, Cambridge, p. 80
Peebles P. J. E., 1980, The Large-Scale Structure of the Universe. Princeton Univ. Press, Princeton

858 *L.-W. Chen et al.*

Persic M., De Zotti G., Boldt E. A., Marshall F. E., Danese L., Franceschini A., Palumbo G. G. C., 1989, ApJ, 336, L47

Plucinsky P. P., Snowden S. L., Briel U. G., Hasinger G., Pfeffermann E., 1993, ApJ, 418, 519

Raymond J. C., Smith B. W., 1977, ApJS, 35, 419

*ROSAT* AO-2 Technical Description, 1991, Rutherford Appleton Laboratory, Oxford

Scheuer P. G., 1974, MNRAS, 167, 329

Shafer R. A., 1983, PhD thesis, Univ. Maryland

Snowden S. L., Freyberg M., 1993, ApJ, 404, 403

Snowden S. L., Plucinsky P. P., Briel U. C., Hasinger G., Pfeffermann E., 1992, ApJ, 393, 819

Snowden S. L., McCammon D., Burrows D. N., Mendenhall J. A., 1993a, preprint

Snowden S. L., Hasinger G., Jahoda K., Lockman F., McCammon D., Sanders W. T., 1993b, preprint

Soltan A. M., 1991, MNRAS, 250, 241

Stark A. A., Gammie C. F., Wilson R. F., Ball J., Linke R. A., Heiles C., Hurwitz M., 1992, ApJS, 79, 77

Totsuji H., Kihara T., 1969, PASJ, 21, 221

Wang Q. D., McCray R., 1993, ApJ, 409, L37

Wu X., Hamilton T., Helfand D. J., 1991, ApJ, 379, 564